RSC Advances

PAPER

View Article Online
View Journal | View Issue

Cite this: *RSC Adv.*, 2022, **12**, 22881

Tuning the catalytic properties of La–Mn perovskite catalyst *via* variation of A- and B-sites: effect of Ce and Cu substitution on selective catalytic reduction of NO with NH_3

Wei Zhang, *[ab] Kang Xie,[ab] Yunhao Tang,[ab] Shan Cheng,[ab] Mengxia Qing,[ab] Yanni Xuan,[ab] Chuan Qin,[ab] Mengyao Dong,[ab] Yunhe Zhou[ab] and Jie Li[ab]

Perovskites with flexible structures and excellent redox properties have attracted considerable attention in industry, and their denitration activities can be further improved with metal substitution. In order to investigate the effect of Ce and Cu substitution on the physicochemical properties of perovskite in NH_3-SCR system, a series of $La_{1-x}Ce_xMn_{1-y}Cu_yO_3$ (x = 0, 0.1, y = 0, 0.05, 0.1, 0.2, 0.4) catalysts were prepared by citrate sol-gel method and employed for NO removal in the simulated flue gas, and the physical and chemical properties of the catalysts were studied using XRD, SEM, BET, XPS, DRIFT characterizations. The Ce substitution on A-site cation of $LaMnO_3$ can improve the denitration activity of the perovskite catalyst, and $La_{0.9}Ce_{0.1}MnO_3$ displays NO conversion of 86.7% at 350 °C. The characterization results indicate that the high denitration activity of $La_{0.9}Ce_{0.1}MnO_3$ is mainly attributed to the larger surface area, which contributes to the adsorption of NH_3 and NO. Besides, the appropriate Cu substitution on B-site cation of $La_{0.9}Ce_{0.1}MnO_3$ can further improve the denitration activity of perovskite catalyst, and $La_{0.9}Ce_{0.1}Mn_{0.8}Cu_{0.2}O_3$ displays the NO conversion of 91.8% at 350 °C. Although the specific surface area of $La_{0.9}Ce_{0.1}Mn_{0.8}Cu_{0.2}O_3$ is lower than $La_{0.9}Ce_{0.1}MnO_3$, the Cu active sites and the Ce^{3+} contents are more developed, making many reaction units formed on the catalyst surface and redox properties of catalyst improved. In addition, strong metal interaction (Ce^{4+} + Mn^{2+} + Cu^{2+} ↔ Ce^{3+} + Mn^{3+}/Mn^{4+} + Cu^{+}) and high concentrations of chemical adsorbed oxygen and lattice oxygen both strengthen the redox reaction on catalyst surface, thus contributing to the better denitration activity of $La_{0.9}Ce_{0.1}Mn_{0.8}Cu_{0.2}O_3$. Therefore, appropriate cerium and copper substitution will markedly improve the denitration activity of La–Mn perovskite catalyst. We also reasonably conclude a multiple reaction mechanism during NH_3-SCR denitration process basing on DRIFT results, which includes the Eley–Rideal mechanism and Langmuir–Hinshelwood mechanism.

Received 2nd July 2022
Accepted 3rd August 2022

DOI: 10.1039/d2ra04085a

rsc.li/rsc-advances

1. Introduction

Nitrogen oxide (NO_x) is one of the thorniest and most widespread environmental pollutants in combustion flue gas produced from automobile exhaust emissions and industrial processes. NO_x is considered a major cause of photochemical smog, ozone depletion, acid rain and the greenhouse effect.[1,2] At present, NO_x emission is regulated and standardized worldwide to minimize the harm to the environment. Selective catalytic reduction of NO_x with NH_3 (NH_3-SCR) is considered to be the most widely-applied and effective denitration technology.[3,4] Typical commercial vanadium-titanium catalysts (V_2O_5/TiO_2 and V_2O_5-WO_3/TiO_2) have been commonly used in many industrial activities due to their stability and high efficiency, but are still restrained by their inevitable drawbacks such as vanadium toxicity, narrow and high operation temperature window, poisoning and deactivation of the catalysts by deposited alkaline metals.[5–7] Moreover, there is an increasing requirement for limiting NO_x emission from industrial applications, which has made the development of NH_3-SCR catalysts with excellent denitration activity a hot issue for decades.

In recent years, transition metal and rare earth metal catalysts have been widely researched for NH_3-SCR systems. Transition metal oxides possess high denitration activity due to their various oxidation states, and rare earth metal oxides have excellent oxygen storage capacity and redox properties. Moreover, perovskite oxides also exhibit good structure stability beyond the above superiorities, thus they have received much attention in the field of NH_3-SCR catalysts. Perovskite oxides

[a]School of Energy and Power Engineering, Changsha University of Science & Technology, Changsha, 410114, China. E-mail: weizhang@csust.edu.cn
[b]Key Laboratory of Renewable Energy Electric-Technology of Hunan Province, Changsha, 410114, China

have a typical chemical formula of ABO_3, where A is a lanthanide or alkaline cation and B is a transition metal cation. The B cation is six-fold coordinated with the oxygen atoms to form BO_6 octahedron, while A cations occupy the voids created by the BO_6 octahedrons.[8] Owning to the presence of BO_6 octahedron, perovskite is capable to maintain the structure stability when A and B cations are partially substituted by other metal ions. This could induce the lattice distortion and symmetry reduction,[9] causing the BO_6 octahedral units change from ideal cubic symmetry to the rhombohedral symmetry or orthorhombic symmetry. The cubic symmetry can provide a larger diffusion space than the rhombohedral or orthorhombic symmetry, making the oxide ions diffuse more easily.[10] While the lattice distortion leads to the formation of abundant oxygen vacancies, promoting the surface oxygen species adsorption and increasing the lattice oxygen migration.[11] Furthermore, lanthanide metal cation substitutes in A-site cation will produce lattice defects and oxygen vacancies, and transition metal cation substitutes in B-site cation will directly changes its oxidation valence state, thus affecting the redox performance of perovskite composite oxides. Therefore, A- and B-sites can be substituted by designated cations with different valences or radius to improve perovskite physicochemical properties for industrial application.[12]

Mn-based catalysts have the multivalent oxidation states mainly including Mn^{2+}, Mn^{3+} and Mn^{4+}, and the mutual conversion of three valence states is crucial to the denitration activity of catalyst in NH_3-SCR reaction.[13,14] Among the Mn-containing catalysts, $LaMnO_3$ has attracted interest with its Mn^{3+}/Mn^{4+} coexisted oxidation state and over-stoichiometric oxygen,[15,16] excessive oxygen always formed to guarantee the lattice electroneutrality of the perovskite due to increasing Mn^{4+} content. The research also shows that copper substitution can promote the generation of oxygen vacancies, so that NO adsorbed on the surface oxygen vacancies can obtain more electrons and be easier to be reduced. Cu partially substitutes Mn ions can lead to the synergistic effect of Cu^{2+} and Mn^{3+}, meanwhile improve the denitration performance of the catalyst.[16] Cerium oxide is usually adopted in the NH_3-SCR catalysts to enhance their denitration activities due to the excellent oxygen storage *via* the redox shift between Ce^{4+} and Ce^{3+}.[17] It has also been reported that chemisorbed oxygen, Mn^{4+} content, NH_3 adsorption capacity and reducibility can be further increased with cerium substitution.[13] Besides, NO oxidation over $LaMnO_{3+\delta}$ catalysts also can be improved by selectively removing the La atoms.[17] Basing on the above information, it is promising and logical to develop NH_3-SCR catalysts by partially replacing La in with cerium, partially replacing Mn with copper and combining the prominent properties of Ce, Cu and perovskite oxides.

In this paper, we have synthesized various $La_{1-x}Ce_xMn_{1-y}Cu_yO_3$ ($x = 0, 0.1, y = 0, 0.05, 0.1, 0.2, 0.4$) catalysts with citrate sol-gel method, and the efficiency of $La_{1-x}Ce_xMn_{1-y}Cu_yO_3$ ($x = 0, 0.1, y = 0, 0.05, 0.1, 0.2, 0.4$) catalysts on the NO removal in simulated flue gas was carried to evaluate the NH_3-SCR catalytic activity. We also investigated the inherent relationships between structure, morphology, surface element composition and catalytic activity of the catalysts. The structure, morphological and redox properties of the catalysts were studied by XRD, SEM, BET and XPS. Besides, the mechanism of denitration reaction on perovskite catalyst surface was discussed with DRIFT results. This study focused on the effects of Ce and Cu substitution on the physicochemical properties and denitration activity of the La–Mn perovskite catalysts and would provide a possibility of controlling the catalytic properties of NH_3-SCR catalysts for industrial application by changing the composition of A- and B-sites of La–Mn perovskite catalysts.

2. Materials and methods

2.1 Catalyst preparation

The series of $La_{1-x}Ce_xMn_{1-y}Cu_yO_3$ ($x = 0, 0.1, y = 0, 0.05, 0.1, 0.2, 0.4$) catalysts were synthesized by the citrate sol-gel method. The chemicals of $La(NO_3)_3 \cdot 6H_2O$ (99%, Macklin, China), $Ce(NO_3)_3 \cdot 6H_2O$ (99.95%, Macklin, China), $Mn(NO_3)_2$ (50 wt% aqueous solution, Macklin, China) and $Cu(NO_3)_2 \cdot 3H_2O$ (99%, Xilong scientific, China) with specific ratios were dissolved in deionized water and mixed with magnetic stirrer. The citric acid (99.5%, Macklin, China) was used as a chelating agent and added into the above solution, where the mole ratio of citric acid to total metal ions was 1.2. Next, the solution was mixed at 90 °C in a magnetic stirrer until yellow viscous gel was formed. Then the gel was dried at 120 °C for 12 h at an oven, and the spongy precursor was obtained. After that, the precursor was ground and calcined at 700 °C for 5 h in a muffle furnace to form the perovskite structure. Additionally, the heating ramp rates of evaporation and calcination were 5 °C min^{-1} and 10 °C min^{-1}, respectively. Finally, the samples were ground and sieved using a 40–60 mesh sieve for catalytic activity tests.

2.2 Catalyst characterization

The X-ray Diffraction (XRD) patterns of the samples were measured in an X'Pert PRO MPD diffractometer (PANalytical, Netherlands) with Cu $K\alpha$ radiation ($\lambda = 0.15406$ nm, 45 kV, 40 mA). The diffraction angle was selected in the 2θ range from 10° to 80° with the scanning rate of 10°/min. The average crystal size was calculated from the Scherrer equation.[6]

The Scanning Electron Microscopy (SEM) images were taken with a Zeiss sigma 300 field emission scanning electron microscope (Carl Zeiss AG, China) to study the morphology of catalysts.

The Brunauer Emmert Teller (BET) surface area and Barrett Joyner Halenda (BJH) pore size distribution of the catalysts were determined by N_2 adsorption-desorption isotherms at −196 °C on a Micromeritics ASAP 2460 surface area and porosity analyzer (Micromeritics, USA) to study the textural properties. Before measurement, the samples were degassed at 300 °C for 6 h in vacuum.

The X-ray Photoelectron Spectroscopy (XPS) measurements were performed on a ESCALAB Xi+ spectrometer (Thermo Fischer, USA) equipped with Al $K\alpha$ radiation serve as excitation source. The binding energies were corrected by C 1s peak at 284.6 eV to compensate the charging effect of all catalysts.

The Diffuse Reflaxions Infrared Fourier Transformations spectroscopy (DRIFT) were carried on Nicolet IS 50 spectrometer (Thermo Fischer, USA) equipped with intelligent collector and MCT/A detector, the scanning range was 4000–400 cm^{-1}.

2.3 Denitration performance experiments

The denitration performance experiments were carried with a fixed-bed reactor in the temperature range of 150–400 °C. Here, 200 mg catalyst (40–60 mesh) was fitted in a quartz tube reactor (i.d. = 12 mm) in each test. The reaction conditions were presented as follows: 500 ppm NO, 500 ppm NH_3, 5% O_2 and N_2 balanced. The total flow rate of the feeding gas was kept at 1000 mL min^{-1}, corresponding to a gas hourly space velocity (GHSV) of 60 000 h^{-1}. During each temperature point, NO concentrations in the inlet and outlet gas were collected with a professional flue gas analyzer (Madur Photon & PGD-100, Austria) after NH_3-SCR reaction was stable for 10 min. NO conversion was calculated according to the following equation:

$$X_{NO} = \frac{C_{NO(in)} - C_{NO(out)}}{C_{NO(in)}} \times 100\%$$

where X_{NO} represents NO conversion, $C_{NO(in)}$ and $C_{NO(out)}$ are the NO concentrations at the inlet and outlet of the quartz tube reactor, respectively.

3. Results and discussion

3.1 Textural analysis basing on XRD results

The phase structures of $La_{1-x}Ce_xMn_{1-y}Cu_yO_3$ ($x = 0, 0.1, y = 0, 0.05, 0.1, 0.2, 0.4$) catalysts were characterized by XRD instrument. As shown in Fig. 1, the diffraction peaks at 23.1°, 32.9°, 40.3°, 47.0°, 52.7°, 58.4°, 68.9°, 78.1° of the catalysts are assigned to the rhombohedral structure of $LaMnO_{3.15}$ (JCPDS #50-0299), meaning that the $LaMnO_{3+\delta}$ perovskite phases with over-stoichiometric oxygen were formed instead of the stoichiometric $LaMnO_3$.[18] The main diffraction peak (2θ = 32.9°) of the catalysts shifts to lower values with the addition of cerium and copper, which indicates that the cell volume become smaller due to the lattice distortion. When La^{3+} (1.17 Å) substituted by Ce^{4+} (0.92 Å) or Ce^{3+} (1.03 Å) with a smaller radius, the average radius of A-site cation of perovskite phase reduced, causing the lower tolerance factor value of crystal structure and leading to the decreased symmetry of perovskite (*i.e.*, lattice distortion).[19] Besides, the radius of Mn ions with +2, +3 and +4 valence are 0.83 Å, 0.65 Å and 0.54 Å, respectively. The radius of Cu ions with +1 and +2 valence are 0.96 Å and 0.73 Å, respectively. Therefore, Mn ions are replaced by Cu ions with higher average ion radius, which also causing the decrease of tolerance factor value and perovskite symmetry. In addition, the intensity of characteristic diffraction peak corresponding to $LaMnO_{3.15}$ perovskite phase in $La_{0.9}Ce_{0.1}Mn_{1-y}Cu_yO_3$ (y = 0, 0.05, 0.1, 0.2, 0.4) catalysts strengthens with the increasement of Cu substitution, indicating that Cu substitution can improve the crystallinity and content of perovskite phase in $La_{0.9}Ce_{0.1}Mn_{1-y}Cu_yO_3$ ($y = 0, 0.05, 0.1, 0.2, 0.4$) catalysts. The diffraction peak ($2\theta = 28.2°$) assigned to the structure of Ce_2O_3 (JCPDS #81-0792) can be observed in $La_{0.9}Ce_{0.1}Mn_{0.95}Cu_{0.05}O_3$ and $La_{0.9}Ce_{0.1}Mn_{0.9}Cu_{0.1}O_3$ catalysts,[20] it is reported that Ce_2O_3 has prominent oxygen storage capacity and high reducibility owing to the redox shifting between Ce^{4+}, Ce^{3+} and oxygen defects, which provides an important promotion effect on the NH_3-SCR activity.[21] However, with the increasement of Cu substitution ratio in the catalyst, the characteristic peak of Ce_2O_3 decreases gradually. The phenomena indicates that there may be strong interaction between Cu and Ce, and the interaction is affected by the amount of Cu substitution in the sample. The characteristic diffraction peak of copper oxide (JCPDS #89-2529) for $La_{0.9}Ce_{0.1}Mn_{0.6}Cu_{0.4}O_3$ catalyst appears at $2\theta = 35.6$ and 38.7°,[22] indicating that a small amount of CuO impurities were formed in $La_{0.9}Ce_{0.1}Mn_{0.6}Cu_{0.4}O_3$ catalyst. Therefore, it is reasonable to conclude that lattice distortion caused by cerium and copper substitution will reduce the symmetry of perovskite phase, thus promoting the formation of oxygen vacancies and the improvement of denitration activity. However, excessive lattice distortion will shrink the diffusion space, making it is unfavorable to the diffusion of oxide ions, which may cause the substantial reduction in denitration activity of catalysts.

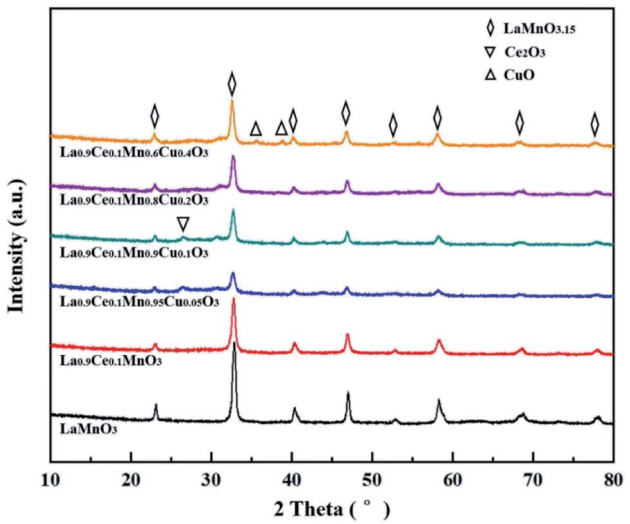

Fig. 1 XRD patterns of $La_{1-x}Ce_xMn_{1-y}Cu_yO_3$ ($x = 0, 0.1, y = 0, 0.05, 0.1, 0.2, 0.4$) catalysts.

Table 1 Lattice parameters of $La_{1-x}Ce_xMn_{1-y}Cu_yO_3$ ($x = 0, 0.1, y = 0, 0.05, 0.1, 0.2, 0.4$) catalysts

Catalysts	V^a (Å^3)	D^b (nm)
$LaMnO_3$	347.21	17.46
$La_{0.9}Ce_{0.1}MnO_3$	346.88	17.20
$La_{0.9}Ce_{0.1}Mn_{0.95}Cu_{0.05}O_3$	349.84	18.27
$La_{0.9}Ce_{0.1}Mn_{0.9}Cu_{0.1}O_3$	353.25	19.41
$La_{0.9}Ce_{0.1}Mn_{0.8}Cu_{0.2}O_3$	352.85	16.71
$La_{0.9}Ce_{0.1}Mn_{0.6}Cu_{0.4}O_3$	348.94	20.99

[a] Determined and calculated from XRD patterns (MDI Jade 6.0 program). [b] Calculated from XRD patterns with the Scherrer equation.

In order to further explore the crystal structure of $La_{1-x}Ce_xMn_{1-y}Cu_yO_3$ ($x = 0$, 0.1, $y = 0$, 0.05, 0.1, 0.2, 0.4) catalysts, the unit cell volume and average crystal size shown in Table 1, which are obtained from XRD results dealt with MDI Jade 6.0 program. It can be observed that the cerium and copper substitution both will lead to the variability of the unit cell volume and average crystal size of catalysts, which are correlated with the lattice distortion and variation of average valence state and radius of A-site and B-site cations in catalysts. On the one hand, the cerium substitution will cause the lattice distortion and reduce the unit cell volume and average crystal size. On the other hand, the copper substitution can cause the change of the average valence state and average radius of Ce, Cu and Mn. Moreover, according to the previous analysis, the increase of average valence state of Ce or the decrease of average valence state of Cu and Mn will reduce the tolerance factor value and aggravate the degree of lattice distortion, and *vice versa*. Therefore, the cerium and copper substitution will change the average valence state and radius of A-site and B-site cations of catalysts, then change the lattice distortion, the unit cell volume and average crystal size of catalysts, thus affecting the denitration performance of catalysts.

3.2 Morphological analysis basing on SEM and BET results

The morphology of $La_{1-x}Ce_xMn_{1-y}Cu_yO_3$ ($x = 0$, 0.1, $y = 0$, 0.05, 0.1, 0.2, 0.4) catalysts was characterized by SEM images, as shown in Fig. 2. The $LaMnO_3$ sample displays a fluffy porous structure with rod-like particles. However, it can be seen that the catalyst particles become smaller and the distances between particles become narrower in $La_{0.9}Ce_{0.1}MnO_3$ compared to $LaMnO_3$. With the partial substitution of Mn ions by Cu ions at B site, the surface morphology of the catalyst still presents porous wool structure in $La_{0.9}Ce_{0.1}Mn_{0.95}Cu_{0.05}O_3$, the metal particles on the catalyst surface gather to a certain extent in $La_{0.9}Ce_{0.1}Mn_{0.9}Cu_{0.1}O_3$, and the aggregation degree of metal particles on the catalyst surface is further intensified in $La_{0.9}Ce_{0.1}Mn_{0.8}Cu_{0.2}O_3$. When the Cu substitution amount reaches 0.4, the surface morphology of the catalyst changes significantly, the porous wool structure basically disappears, and the catalyst particles obviously gather in local areas, which reduces the dispersion of active sites, thus decreasing the denitration efficiency of catalyst.

The N_2 adsorption-desorption isotherms and BJH pore size distributions of catalysts are shown in Fig. 3 and 4, respectively. It is possible to observe that $LaMnO_3$ and $La_{0.9}Ce_{0.1}MnO_3$ catalysts all present typical type IV isotherms with type H4 hysteresis loop at $P/P_0 = 0.6$–1.0. According to IUPAC classifications, type IV isotherms are exhibited by the mesoporous materials, and type H4 hysteresis loop can be attributed to the capillary condensation of nitrogen molecules in the

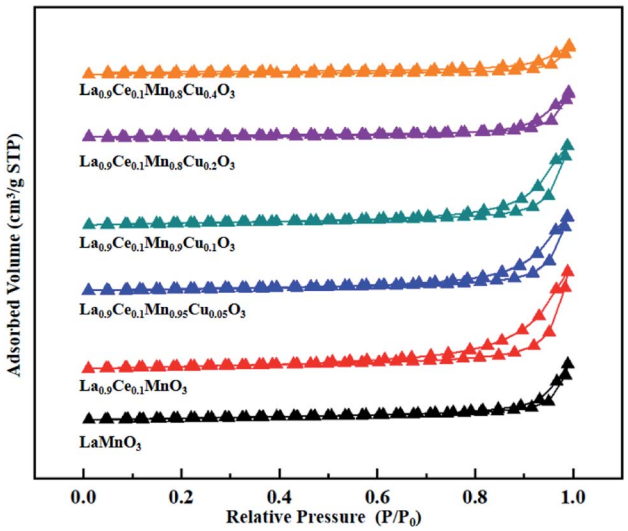

Fig. 3 N_2 adsorption-desorption isotherms of $La_{1-x}Ce_xMn_{1-y}Cu_yO_3$ ($x = 0$, 0.1, $y = 0$, 0.05, 0.1, 0.2, 0.4) catalysts.

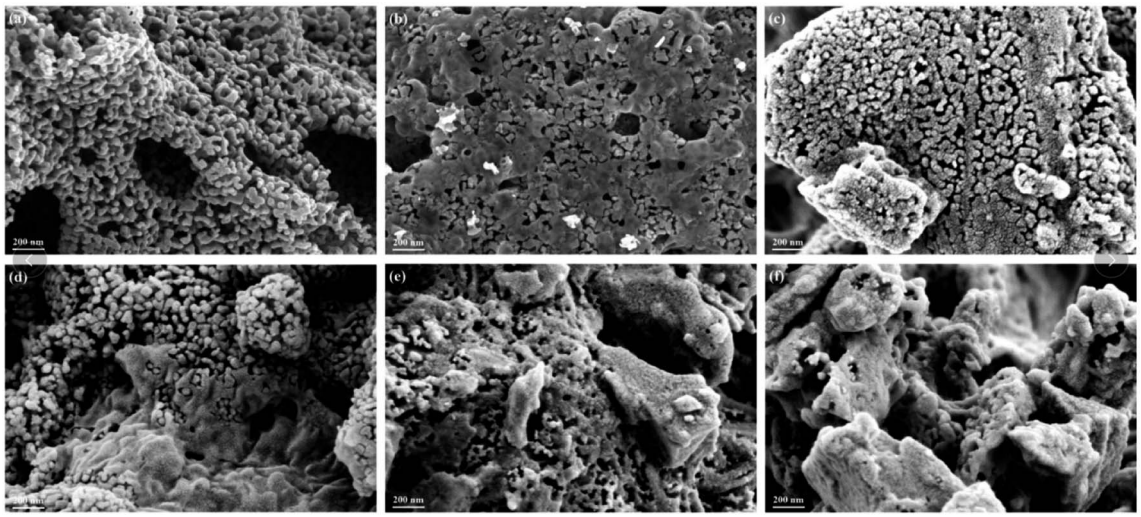

Fig. 2 SEM images of (a) $LaMnO_3$, (b) $La_{0.9}Ce_{0.1}MnO_3$, (c) $La_{0.9}Ce_{0.1}Mn_{0.95}Cu_{0.05}O_3$ and (d) $La_{0.9}Ce_{0.1}Mn_{0.9}Cu_{0.1}O_3$, (e) $La_{0.9}Ce_{0.1}Mn_{0.8}Cu_{0.2}O_3$, (f) $La_{0.9}Ce_{0.1}Mn_{0.6}Cu_{0.4}O_3$.

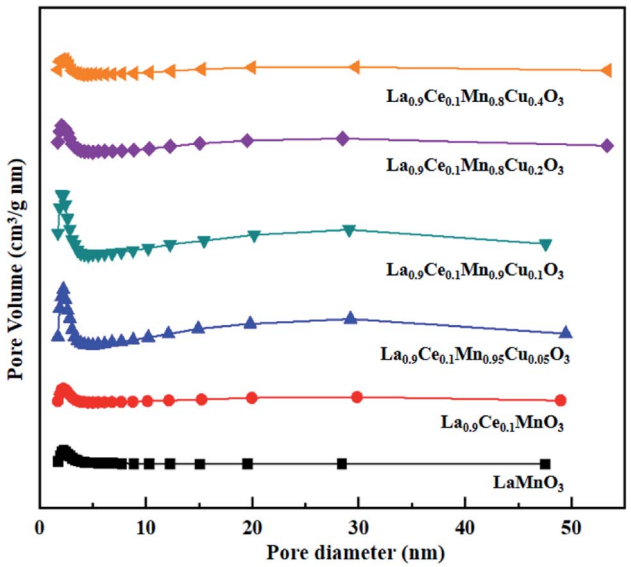

Fig. 4 BJH pore size distributions of $La_{1-x}Ce_xMn_{1-y}Cu_yO_3$ ($x = 0, 0.1, y = 0, 0.05, 0.1, 0.2, 0.4$) catalysts.

mesoporous structure.[23,24] Besides, pore size distributions obtained by BJH method show mesopores mainly in the range of 2–3 nm. Therefore, $LaMnO_3$ and $La_{0.9}Ce_{0.1}MnO_3$ catalysts both have many mesoporous structures. The BET surface area and pore structure of the catalysts are summarized in Table 2. Compared with the $LaMnO_3$ catalyst, the surface area and pore structure of the $La_{0.9}Ce_{0.1}MnO_3$ catalyst increase, which may be related to the decrease of crystal size caused by lattice distortion. With the addition of Cu substitution, the N_2 adsorption desorption isotherms of $La_{0.9}Ce_{0.1}Mn_{0.95}Cu_{0.05}O_3$ and $La_{0.9}Ce_{0.1}Mn_{0.9}Cu_{0.1}O_3$ catalysts are type IV curves with H4 hysteresis loops, indicating that these two catalysts have many mesoporous structures. However, when the Cu substitution ratio reaches 0.2 and 0.4, the hysteresis loop area is significantly reduced and even disappeared, indicating that the high Cu substitution content leads to the reduce in mesoporous structure of catalysts, which is consistent with the SEM results. The reason is that high Cu substitution amount will lead to obvious aggregation of metal particles on the catalyst surface, and the wool porous structure will be transformed into sharp catalyst agglomerates. Therefore, high Cu substitution will significantly destroy the mesoporous structure and reduce the dispersion of active sites on catalysts surface. In addition, the average pore size of the $La_{0.9}Ce_{0.1}Mn_{1-y}Cu_yO_3$ ($y = 0, 0.05, 0.1, 0.2, 0.4$) catalyst sample first decreases and then increases with the increase of Cu substitution amount, which is related to the cluster phenomenon on the catalyst surface. Therefore, Cu partially substitute in $La_{0.9}Ce_{0.1}MnO_3$ catalyst will change the average pore size of the catalyst, and then affect the denitration performance of perovskite catalysts.

In summary, the increase of Cu substitution leads to the reduction in mesoporous structure content, decreases the dispersion of active sites and increases the amount of Cu active sites on catalyst surface. $La_{0.9}Ce_{0.1}Mn_{0.9}Cu_{0.1}O_3$ catalyst and $La_{0.9}Ce_{0.1}Mn_{0.8}Cu_{0.2}O_3$ catalyst both have many mesoporous structure, large specific surface area and high Cu active sites content, which can promote the adsorption of NH_3, NO and other reaction gases on catalyst surface, thus improving the denitration activity of perovskite catalyst.

Table 2 BET surface area and pore structure of $La_{1-x}Ce_xMn_{1-y}Cu_yO_3$ ($x = 0, 0.1, y = 0, 0.05, 0.1, 0.2, 0.4$) catalysts

Catalysts	BET surface area ($m^2\ g^{-1}$)	Pore volumn ($cm^3\ g^{-1}$)	Average pore diameter (nm)
$LaMnO_3$	20.7	0.04	3.63
$La_{0.9}Ce_{0.1}MnO_3$	29.5	0.07	4.83
$La_{0.9}Ce_{0.1}Mn_{0.95}Cu_{0.05}O_3$	22.7	0.06	9.94
$La_{0.9}Ce_{0.1}Mn_{0.9}Cu_{0.1}O_3$	24.7	0.06	9.43
$La_{0.9}Ce_{0.1}Mn_{0.8}Cu_{0.2}O_3$	11.8	0.03	9.93
$La_{0.9}Ce_{0.1}Mn_{0.6}Cu_{0.4}O_3$	7.0	0.02	9.94

3.3 Redox properties analysis basing on XPS results

The XPS characterization was used to explore the metallic chemical state and active oxygen species on the perovskite surface. La 3d curves of the catalysts shown in Fig. 5(a), the La $3d_{5/2}$ peaks are located at 833.9 and 838.2 eV, and the La $3d_{3/2}$ peaks are located at 850.7 and 855.0 eV. Therefore, the spin-orbit splitting of the La 3d level is 16.8 eV for all samples, the value observed for the $La_{1-x}Ce_xMn_{1-y}Cu_yO_3$ ($x = 0, 0.1, y = 0, 0.05, 0.1, 0.2, 0.4$) catalysts is very closed to the metallic values of pure lanthanum oxide (La_2O_3), indicating that the La ions are exhibited in trivalent state for all catalysts.[25]

The obtained Ce 3d spectra are represented in Fig. 5(b). Eight components can be obtained by fitting the curves, the four characteristic peaks at 882.1 eV, 885.0 eV, 889.1 eV and 898.1 eV are represented by v, v′, v″and v‴, while the other four characteristic peaks at 901.2 eV, 903.8 eV, 907.8 eV and 916.4 eV are represented by u, u′, u″ and u‴.[26] The peaks denoted as v′, u′ are assigned to Ce^{3+} species with $3d^{10}\ 4f^1$ initial electronic configuration, while the peaks denoted as u, u″, u‴, v, v″ and v‴ are attributed to the $3d^{10}\ 4f^0$ electronic state corresponding to Ce^{4+}.[27] It shows that Ce^{3+} and Ce^{4+} coexist on cerium containing catalysts surfaces, and the formed Ce^{4+}/Ce^{3+} redox couple is promotional for the improvement of denitration activity.

Fig. 5(c) shows the Mn 2p spectra of the six catalysts, two main peaks due to Mn $2p_{3/2}$ and Mn $2p_{1/2}$ are found in the figure, and both of them can be well fitted into three peaks assigned to Mn^{2+}, Mn^{3+} and Mn^{4+} species. Among these six peaks, the peaks at 640–641 and 652–653 eV are denoted as Mn^{2+} ions, the peaks at 641–642 and 653–654 eV are identified as Mn^{3+}, and the peaks at 644–645 and 656–657 eV are attributed to Mn^{4+}.[17] Besides, it can be seen from the figure that the peak areas corresponding to different Mn valence states change with the increase of the Cu substitution proportion, indicating that there is a synergistic effect between Cu and Mn on catalyst surface.

Fig. 5(d) shows the Cu 2p spectra of $La_{0.9}Ce_{0.1}Mn_{1-y}Cu_yO_3$ ($y = 0, 0.05, 0.1, 0.2, 0.4$) catalysts, two main peaks of Cu $2p_{3/2}$ and Cu $2p_{1/2}$ are found in the figure. The characteristic peaks near

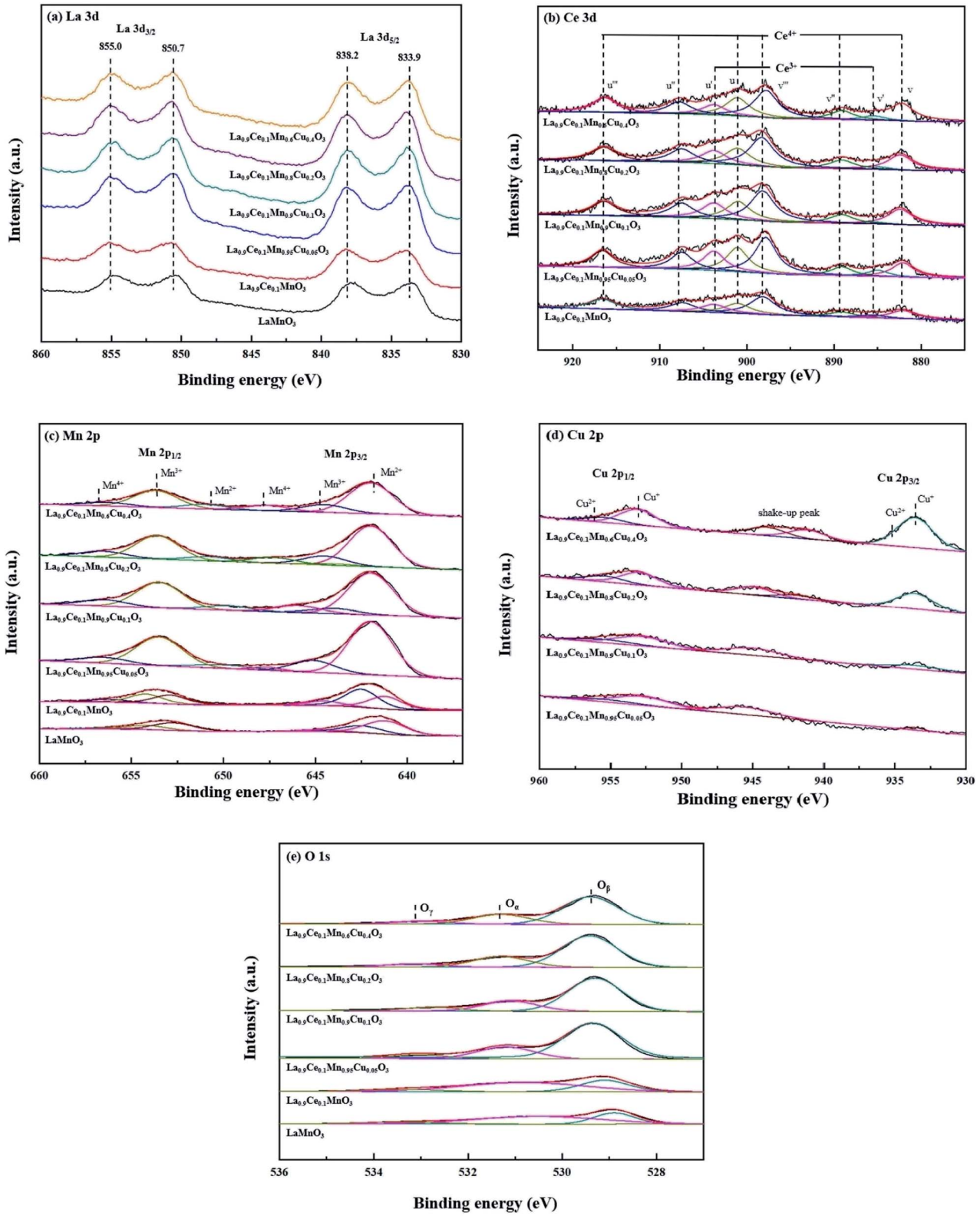

Fig. 5 XPS spectra of $La_{1-x}Ce_xMn_{1-y}Cu_yO_3$ ($x = 0, 0.1$, $y = 0, 0.05, 0.1, 0.2, 0.4$) catalysts: (a) La 3d, (b) Ce 3d, (c) Mn 2p, (d) Cu 2p, (e) O 1s.

933.6 eV and 953.1 eV belong to Cu^+, the characteristic peaks near 935.4 eV and 955.7 eV belong to Cu^{2+}, and the vibrational satellite peaks between 940-947 eV also confirm the existence of Cu^{2+} and polycrystalline Cu_2O substances in the four catalyst samples.[28,29] In addition, it can be seen from the Fig. 5(d) that along with the Cu substitution increases, the width and height

of the above characteristic peaks gradually increase, indicating that the Cu content increases significantly. At the same time, the characteristic peak areas corresponding to Cu^{2+} and Cu^{+} also change in different degrees, indicating that the change of Cu average valence state.

The O 1s spectra of $La_{1-x}Ce_xMn_{1-y}Cu_yO_3$ ($x = 0$, 0.1, $y = 0$, 0.05, 0.1, 0.2, 0.4) catalysts are shown in Fig. 5(e). The peak at 529.4 eV belongs to the lattice oxygen (O_β) of the catalyst, the peak at 531.3 eV represents the surface chemically adsorbed oxygen (O_α), while the peak at 533.0 eV belongs to the bulk lattice oxygen (O_γ),[30] and their promotion degrees on the denitration activity of the catalyst are different. Therefore, it also can be seen from the Fig. 5(e) that the corresponding characteristic peaks areas of the three active oxygen species are different, leading to the different denitration efficiency of the four catalysts.

The chemical valence content of surface elements of $La_{1-x}Ce_xMn_{1-y}Cu_yO_3$ ($x = 0$, 0.1, $y = 0$, 0.05, 0.1, 0.2, 0.4) catalysts are shown in Table 3. It can be observed that the oxidation valence states of Ce, Mn and Cu in $La_{1-x}Ce_xMn_{1-y}Cu_yO_3$ ($x = 0$, 0.1, $y = 0$, 0.05, 0.1, 0.2, 0.4) catalysts change along with the increase of Cu substitution. When the Cu substitution ratio at the range of 0.05–0.2, the addition of Cu substitution is accompanied with the decrease in the proportion of Mn^{2+} and the increase in the proportion of Ce^{3+} and Cu^{+}. However, $La_{0.9}Ce_{0.1}Mn_{0.6}Cu_{0.4}O_3$ has higher Mn^{2+} concentration and lower Ce^{3+} concentration than that of $La_{0.9}Ce_{0.1}Mn_{0.6}Cu_{0.4}O_3$. The above phenomena shows that the decrease of the average valence state of Ce and Cu is accompanied by the increase of the average valence state of Mn. Therefore, there may be exist a synergetic effect among Ce, Mn and Cu, and the effect is inhibited at the moment of excessive Cu substitution. The probable synergetic effect as follows:[31]

$$Ce^{4+} + Mn^{2+} + Cu^{2+} \leftrightarrow Ce^{3+} + Mn^{3+} + Cu^{+}$$

$$Ce^{4+} + Mn^{2+} + Cu^{2+} \leftrightarrow Ce^{3+} + Mn^{4+} + Cu^{+}$$

According to the chemical valence content of metal elements on the catalyst surface in Table 3, it is reasonable to conclude the above synergetic effect among Ce, Mn and Cu affected by the Cu substitution. When the Cu substitution proportion reaches 0.2, the interaction is the strongest, and the number of electrons transferred between metal elements is the largest, which is conducive to the redox reaction of the gas adsorbed on the catalyst surface. Besides, it can be seen from table that the $La_{0.9}Ce_{0.1}Mn_{0.8}Cu_{0.2}O_3$ has the highest Ce^{3+} content. Ce^{3+} has been reported that it can originate oxygen vacancies, charge imbalance and unsaturated chemical bonds,[32] thus promoting to improve the redox capacity and the denitration efficiency of the catalyst. The research shows that the high proportion of high Mn valence state can promote the redox reaction on the catalyst surface, and then significantly improve the low-temperature denitration activity of the catalyst.[33] It can be seen from Table 3 that the order of $(Mn^{3+} + Mn^{4+})/Mn^{n+}$ of Cu-doped catalysts is $La_{0.9}Ce_{0.1}Mn_{0.8}Cu_{0.2}O_3$ > $La_{0.9}Ce_{0.1}Mn_{0.9}Cu_{0.1}O_3$ > $La_{0.9}Ce_{0.1}Mn_{0.6}Cu_{0.4}O_3$ > $La_{0.9}Ce_{0.1}Mn_{0.95}Cu_{0.05}O_3$, the average valence state of Mn ions in $La_{0.9}Ce_{0.1}Mn_{0.8}Cu_{0.2}O_3$ catalyst is the highest, which is conducive to the enhancement of its denitration activity.

In addition, the surface chemically adsorbed oxygen and the lattice oxygen are the important active oxygen of NH_3-SCR denitration reaction, which both assist to enhance the low-temperature denitration activity of the catalyst. It is reported that O_2 takes part in the NH_3-SCR reaction *via* taking up the oxygen vacancies of catalyst surface,[34] and the lattice oxygen and chemical adsorbed oxygen are compensated in the process. Therefore, the oxygen vacancy also has important role in the denitration activity, and we can utilize the sum of O_α and O_β to quantify oxygen vacancies in catalysts. It can be seen that cerium and copper substitution both can increase the proportion of (O_α + O_β), and $La_{0.9}Ce_{0.1}Mn_{0.8}Cu_{0.2}O_3$ has the highest proportion of (O_α + O_β), which may be helpful to the NH_3-SCR denitration activity. Besides, the proportion of (O_α + O_β) is related to the content of Ce^{3+}, (Mn^{3+} + Mn^{4+}) and Cu^{+} in varying degrees, indicating that the proportion of (O_α + O_β) has a correlation with the synergetic effects among Ce, Mn and Cu, thus jointly promoting the improvement of denitration efficiency.

In conclusion, there is synergetic effect among Ce, Mn and Cu metal ions in the process of Cu substitution, which reduces the average valence state of Ce and Cu and increases the average valence state of Mn, and promotes the formation of the chemical adsorbed oxygen and lattice oxygen, thus affecting the redox ability and denitration performance of perovskite catalysts.

3.4 NH_3-SCR activity

NO conversions of $La_{1-x}Ce_xMn_{1-y}Cu_yO_3$ ($x = 0$, 0.1, $y = 0$, 0.05, 0.1, 0.2, 0.4) catalysts in the simulated flue gas at the

Table 3 Surface atomic ratios of different species over $La_{1-x}Ce_xMn_{1-y}Cu_yO_3$ ($x = 0$, 0.1, $y = 0$, 0.05, 0.1, 0.2, 0.4) catalysts

	Ce (%)		Mn (%)			Cu (%)		O (%)		
Catalysts	Ce^{3+}	Ce^{4+}	Mn^{2+}	Mn^{3+}	Mn^{4+}	Cu^{+}	Cu^{2+}	O_α	O_β	O_γ
$LaMnO_3$	—	—	60.6	31.6	7.8	—	—	62.3	29.0	8.7
$La_{0.9}Ce_{0.1}MnO_3$	15.7	84.3	38.5	47.9	13.6	—	—	59.5	32.4	8.1
$La_{0.9}Ce_{0.1}Mn_{0.95}Cu_{0.05}O_3$	17.9	82.1	53.4	39.0	7.6	77.9	22.1	23.7	68.8	7.5
$La_{0.9}Ce_{0.1}Mn_{0.9}Cu_{0.1}O_3$	32.4	67.6	51.2	34.2	14.6	79.9	20.1	21.7	70.5	7.8
$La_{0.9}Ce_{0.1}Mn_{0.8}Cu_{0.2}O_3$	33.3	66.7	50.5	36.4	13.1	82.7	17.3	23.4	69.8	6.8
$La_{0.9}Ce_{0.1}Mn_{0.6}Cu_{0.4}O_3$	32.4	67.6	51.3	35.6	13.1	89.8	10.2	24.6	68.5	6.9

temperature between 150 °C and 400 °C are presented in Fig. 6. It can be seen from the figure that $La_{0.9}Ce_{0.1}MnO_3$ displays higher denitration activity compared with $LaMnO_3$, and NO conversion reaches 86.7% at 350 °C, which shows the Ce substitution can promote to strengthen the denitration activity of La–Mn perovskite catalyst. In addition, the denitration efficiencies of $La_{0.9}Ce_{0.1}Mn_{0.95}Cu_{0.05}O_3$ and $La_{0.9}Ce_{0.1}Mn_{0.6}Cu_{0.4}O_3$ catalysts decrease in varying degrees compared with $La_{0.9}Ce_{0.1}MnO_3$ catalyst, indicating that over lowing or excessive high Cu substitution are both not conducive to improving the denitration performance of the catalyst. Besides, the NO conversion of $La_{0.9}Ce_{0.1}Mn_{0.8}Cu_{0.2}O_3$ catalysts is the highest among the catalysts and reaches 91.8% at 350 °C, indicating that the saturation point of the Cu substitution ratio is around 0.2. Therefore, appropriate cerium and copper substitution will markedly improve the denitration activity of La–Mn perovskite catalyst.

According to the above characterization results, it is reasonable to conclude existence of the inherent relationships between structure, morphology, surface element composition and catalytic activity of the $La_{1-x}Ce_xMn_{1-y}Cu_yO_3$ ($x = 0, 0.1, y = 0, 0.05, 0.1, 0.2, 0.4$) perovskite catalysts. The high denitration activity of $La_{0.9}Ce_{0.1}MnO_3$ is mainly attributed to its many mesoporous structure and large surface area, which contribute to the adsorption of NH_3 and NO. $La_{0.9}Ce_{0.1}Mn_{0.8}Cu_{0.2}O_3$ catalyst has high Cu active sites content, highest proportion of Ce^{3+} and high Mn valence state, strong metal interaction and high concentration of chemical adsorbed oxygen and lattice oxygen, so it has the best denitration activity in the $La_{1-x}Ce_xMn_{1-y}Cu_yO_3$ ($x = 0, 0.1, y = 0, 0.05, 0.1, 0.2, 0.4$) perovskite catalysts.

The comparison of the denitration performance of modified La–Mn perovskite catalysts prepared in this paper with copper-based catalysts, cerium-based catalysts and other reported La–Mn perovskite catalysts have been studied in Table 4. It can be seen that whether copper oxide and cerium oxide alone as catalyst, copper oxide and cerium oxide supported with other catalyst or copper oxide and cerium oxide combine with other materials to form mixture as catalyst, they all show worse denitration efficiency compared with $La_{0.9}Ce_{0.1}Mn_{0.8}Cu_{0.2}O_3$, indicating that the catalyst with perovskite phase has preferable denitration property. Besides, the NH_3-SCR activity of La–Mn perovskite catalyst can be improved by supported with other catalyst, and the A-site and B-site of La–Mn perovskite catalyst substituted with other metal element also can achieve high denitration efficiency. Therefore, we can take other modification methods to further improve the denitration performance of La–Mn perovskite catalysts, thus providing a prospect for further enhancing the denitration efficiency of NH_3-SCR catalysts in industrial denitration application.

Table 4 Comparison of NO conversion of various catalysts

Catalysts	Best NO conversion	Ref.
$La_{0.9}Ce_{0.1}Mn_{0.8}Cu_{0.2}O_3$	91.8% (350 °C)	This work
CuO	<70% (200 °C)	35
CeO_2	<60% (350 °C)	36
Cu/TiO_2–ZrO_2	<80% (400 °C)	2
Ce/TiO_2–ZrO_2	<85% (400 °C)	2
Cu–Ce/Al_2O_3	87.9% (250 °C)	37
Cu_4AlO_x	91.1% (200 °C)	37
CeNTs	85% (350 °C)	38
$LaMnO_3/TiO_2$	>90% (300 °C)	39
$La_{0.9}Sr_{0.1}MnO_3$	<90% (300 °C)	39
$LaMn_{0.95}V_{0.05}O_3$	90% (250 °C)	39

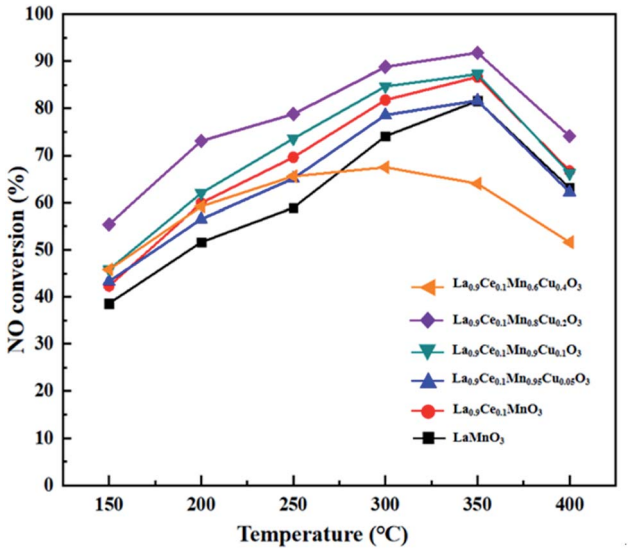

Fig. 6 NO conversion of the $La_{1-x}Ce_xMn_{1-y}Cu_yO_3$ ($x = 0, 0.1, y = 0, 0.05, 0.1, 0.2, 0.4$) catalysts.

3.5 NH_3-SCR reaction mechanism analysis basing on DRIFT results

The $La_{0.9}Ce_{0.1}Mn_{0.8}Cu_{0.2}O_3$ catalyst with the best denitration activity was selected for *in situ* DRIFT characterization to identify the active sites, the adsorbed species and the intermediates on the catalyst surface in the denitration process, aiming at figuring out the reaction mechanism of La–Mn perovskite catalyst in low temperature NH_3-SCR system.

The $La_{0.9}Ce_{0.1}Mn_{0.8}Cu_{0.2}O_3$ catalyst was pre-adsorbed with 500 ppm NH_3 on the surface at 200 °C for 30 min, and then exposed at 500 ppm NO and 5% O_2 for 30 min. The DRIFT spectrum of the catalyst is shown in Fig. 7. The vibrational peaks located at 1042, 1087, 1123, 1234 and 1626 cm^{-1} in the figure are attributed to the coordinating NH_3 on the Lewis acid site, while the vibrational peak at 1397 cm^{-1} belongs to the NH_4^+ adsorption on the Brønsted acid site.[40] The peak intensities of the above vibration peaks decrease with time after the introduction of NO and O_2, indicating that both coordinated NH_3 and NH_4^+ can participate in the NH_3-SCR denitration reaction. In addition, the vibration peak located at 1028, 1503, 1610, 1846 and 1908 cm^{-1} are not reflected in the spectrum after NH_3 pre-adsorption for 30 min, but appear after NO and O_2 purged into the catalyst surface, the peak intensity increases and tends to be stable. Among them, the vibration peak at 1028 cm^{-1} belongs to the *cis*-$N_2O_2^{2-}$ species,[41] and the vibration peak at 1503 cm^{-1} belongs to the amide species ($-NH_2$).[42] The above vibration peaks correspond to the species belong to the

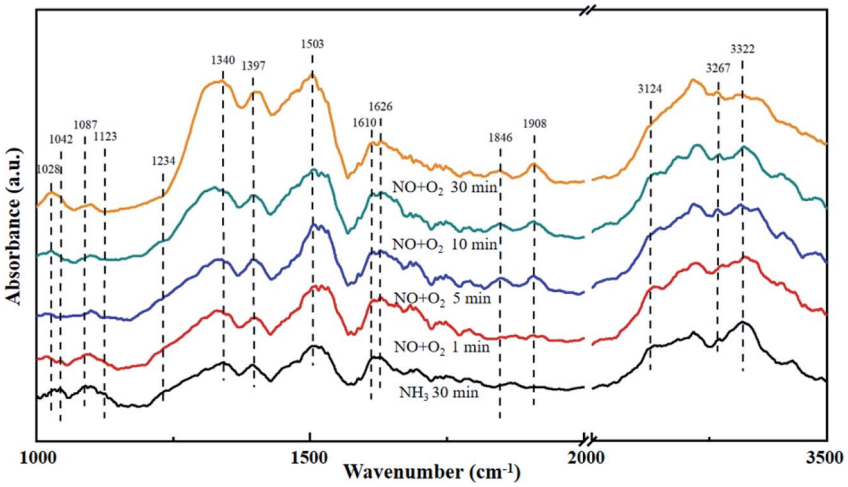

Fig. 7 DRIFT spectra of $La_{0.9}Ce_{0.1}Mn_{0.8}Cu_{0.2}O_3$ exposed to NO at various temperatures. Reaction condition: [NH_3] = [NO] = 500 ppm, [O_2] = 5%, and N_2 balance.

reduction product of NO and the oxidation product of NH_3, respectively, which are important intermediate products of the NH_3-SCR denitration reaction. Meanwhile, the vibrational peak at 1610 cm^{-1} represents NO_2 adsorbed on the catalyst surface,[43] while the vibrational peaks at 1846 and 1908 cm^{-1} represent the adsorbed NO_x species.[44] The vibrational peak at 1340 cm^{-1} is attributed to the monodentate nitrate,[40] and the peak intensity increases significantly after NO and O_2 introduced, indicating that the NH_3-SCR denitration reaction mechanism on the catalyst surface follows the L–H mechanism. Besides, three vibrational peaks appear at 3124, 3267 and 3322 cm^{-1}, which belong to the N–H vibrational region (3000–3500 cm^{-1}), and these peaks also correspond to the coordination NH_3 on the Lewis acid site.[41] The peak intensities of the three vibration peaks weaken along with the NO and O_2 purging, indicating that the NH_3-SCR denitration reaction mechanism on the catalyst surface follows E–R mechanism. Moreover, many Lewis acid sites on the catalyst surface can adsorb a large amount of reaction gas to participate in the NH_3-SCR denitration reaction, which is beneficial to improve the denitration efficiency of lanthanum manganese perovskite catalysts.

The $La_{0.9}Ce_{0.1}Mn_{0.8}Cu_{0.2}O_3$ catalyst was pre-adsorbed with 500 ppm NO and 5% O_2 on the surface at 200 °C for 30 min, and then exposed at 500 ppm NH_3 for 30 min. The DRIFT spectrum of the catalyst is shown in Fig. 8. The vibrational peak at 1038 cm^{-1} represents the *cis*-$N_2O_2^{2-}$ species,[41] the vibrational peak at 1628 cm^{-1} represents the NO_2 adsorbed on the catalyst surface,[45] and the vibrational peaks at 1695 and 1746 cm^{-1} represent NO (M–N=O) adsorbed on the catalyst surface with covalent bond formation,[41] all above peaks represent the intermediate products formed by NO adsorption on the catalyst surface. In addition, the vibrational peaks at 1302, 1508 and 1610 cm^{-1} belong to monodentate nitrate,[43,46] the vibrational peak at 1522 cm^{-1} belongs to bidentate nitrate, the characteristic peak at 1487 cm^{-1} belongs to NH_4^+ adsorbed on the Brønsted acid site, while the characteristic peaks at 3141, 3253 and 3341 cm^{-1} belong to the coordinated NH_3 adsorbed on the Lewis acid site.[46] The peak intensity of the above characteristic peaks increases with the increase of NH_3 purging time, indicating that there are many Brønsted acid sites and Lewis acid sites can participate in the denitration reaction on the catalyst surface, thereby improving the denitration efficiency of the lanthanum manganese perovskite catalyst.

According to the DRIFT characterization results of NH_3 pre-adsorption and NO + O_2 adsorption experiments as well as NO + O_2 pre-adsorption and NH_3 adsorption experiments on the surface of $La_{0.9}Ce_{0.1}Mn_{0.8}Cu_{0.2}O_3$ catalyst, it can be seen that the adsorption of NH_3 on the catalyst surface is very strong at 200 °C, mainly generate coordinating NH_3 on Lewis acid site and NH_4^+ on Brønsted acid site, which can be dehydrogenated into amide species (–NH_2). Besides, NO not only can react with –NH_2 directly, but also can be adsorbed on the catalyst surface and converted into monodentate and bidentate nitrates, which are further combined with NH_4^+ adsorbed on the acid site and finally converted into N_2O and H_2O for the purpose of denitration. In conclusion, the low-temperature NH_3-SCR denitration reaction mechanism on the surface of $La_{0.9}Ce_{0.1}Mn_{0.8}Cu_{0.2}O_3$ catalyst includes E–R mechanism and L–H mechanism.

The adsorption and conversion process of NH_3 on the catalyst surface are as follows:

$$NH_3(g) \rightarrow NH_3(a)\ (\text{Lewis acid sites}) \rightarrow -NH_2(a)$$

$$NH_3(g) \rightarrow NH_4^+(a)\ (\text{Brønsted acid sites}) \rightarrow -NH_2(a)$$

The adsorption and conversion process of NO on the catalyst surface are as follows:

$$NO(g) + O(a) \rightarrow NO_2(a)$$

$$M^{(n-1)+} + O(a) \rightarrow M^{n+}\text{–}O$$

$$M^{n+}\text{–}O + NO_2(a) \rightarrow M^{(n-1)+} + NO_3^-$$

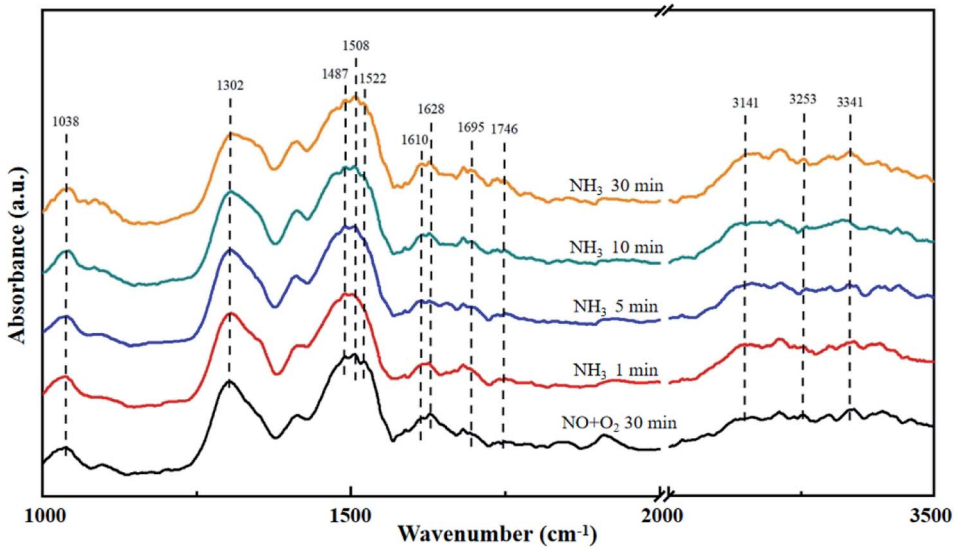

Fig. 8 DRIFT spectra of $La_{0.9}Ce_{0.1}Mn_{0.8}Cu_{0.2}O_3$ exposed to NH_3 at various temperatures. Reaction condition: [NH_3] = [NO] = 500 ppm, [O_2] = 5%, and N_2 balance.

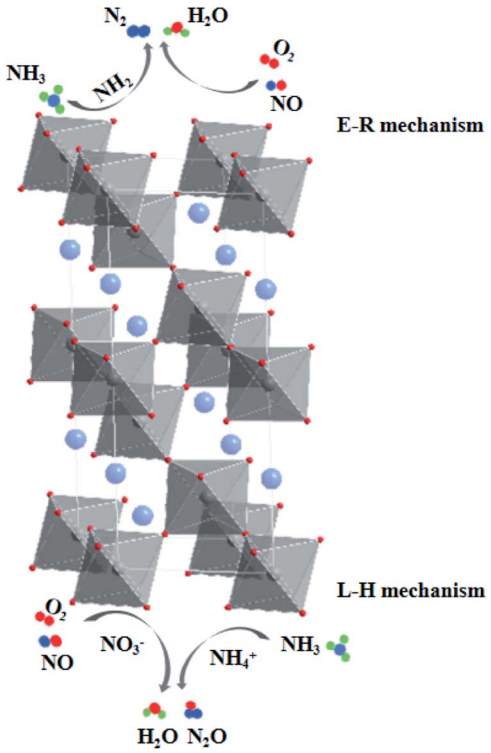

Fig. 9 Mechanism of NH_3-SCR Denitrification on Lanthanum–Manganese Perovskite Catalyst Surface at 200 °C.

The Eley–Rideal denitration reaction mechanism is as follows:

$$-NH_2(a) + NO(g) \rightarrow NH_2NO(a) \rightarrow N_2 + H_2O$$

The Langmuir–Hinshelwood denitration reaction mechanism is as follows:

$$NH_4^+ + NO_3^- \rightarrow NH_4NO_3 \rightarrow N_2O + H_2O$$

As the final summarize comment, the multiple reaction mechanism herein proposed. The multiple reaction mechanism (shown in Fig. 9) on catalyst surface includes Eley–Rideal reaction mechanism and Langmuir–Hinshelwood reaction mechanism, which both promote to improve the denitration activity of La–Mn perovskite catalyst.

4. Conclusions

In the present work, a series of $La_{1-x}Ce_xMn_{1-y}Cu_yO_3$ ($x = 0$, 0.1, $y = 0$, 0.05, 0.1, 0.2, 0.4) catalysts were synthesized by the citrate sol-gel method and characterized by XRD, SEM, BET, XPS and DRIFT techniques. The catalytic activity tests of selective catalytic reduction of NO with NH_3 were carried and the effects of catalyst properties on NH_3-SCR denitration activity were studied. The results show that Ce substitution has a positive impact on improving the denitration activity of $LaMnO_3$ perovskite catalyst, and $La_{0.9}Ce_{0.1}MnO_3$ displays the activity with a maximum NO conversion of 86.7% at 350 °C. The high denitration activity of $La_{0.9}Ce_{0.1}MnO_3$ is mainly attributed to the larger surface area, which promotes to the adsorption of NH_3 and NO. Moreover, the $La_{0.9}Ce_{0.1}MnO_3$ perovskite catalyst was modified with copper substitution. It is found that when the Cu substitution ratio reaches 0.2, the catalyst has the strongest denitration activity, and the NO conversion at 350 °C reaches 91.8%. Although the specific surface area of $La_{0.9}Ce_{0.1}Mn_{0.8}Cu_{0.2}O_3$ is lower than $La_{0.9}Ce_{0.1}MnO_3$, the Cu active sites and the Ce^{3+} content are more developed, making many reaction units formed on the catalyst surface and redox properties of catalyst improved. In addition, strong metal interaction ($Ce^{4+} + Mn^{2+} + Cu^{2+} \leftrightarrow Ce^{3+} + Mn^{3+}/Mn^{4+} + Cu^{+}$) and high concentrations of chemical adsorbed oxygen and lattice oxygen both

assist to strengthen the redox reaction on catalyst surface, thus further improve the denitration activity of perovskite catalyst. Therefore, appropriate cerium and copper substitution will markedly improve the denitration activity of La–Mn perovskite catalyst. We also reasonably conclude a multiple reaction mechanism during NH_3-SCR denitration process, which includes the Eley–Rideal mechanism and Langmuir–Hinshelwood mechanism.

Author contributions

Wei Zhang: conceptualization, methodology, software, resources, data curation, supervision, project administration, funding acquisition. Kang Xie: formal analysis, writing-original draft, writing-review & editing, funding acquisition. Yunhao Tang: investigation, visualization, validation. Shan Cheng: writing-review & editing, funding acquisition. Mengxia Qing: writing-review & editing, funding acquisition. Yanni Xuan: writing-review & editing, funding acquisition. Chuan Qin: investigation, visualization. Mengyao Dong: investigation, validation. Yunhe Zhou: investigation, validation. Jie Li: investigation, validation.

Conflicts of interest

There are no conflicts of interest to declare.

Acknowledgements

This work was supported by the National natural science foundation of China (52006016, 52104391), State scholarship fund awarded by China scholarship (201808430112), Natural science foundation of Hunan province (2020JJ4098, 2021JJ40573), Key projects of scientific research project of Hunan Provincial Department of Education (21A0216), Changsha Municipal Natural Science Foundation (kq2014104), Young teachers growth plan project of CSUST (2019QJCZ044), Key laboratory of renewable energy electric technology of Hunan province (2016ZNDL005, 2018ZNDL004, 2020ZNDL001), 2022 Graduate research and innovation project at Changsha University of Science and Technology (CXCLY2022092).

References

1 D. Wang, B. Huang, Z. Shi, H. Long, L. Li, Z. Yang and M. Dai, *RSC Adv.*, 2021, **11**, 18458, DOI: **10.1039/d1ra02352g**.
2 W. Zhang, Y. Tang, W. Xiao, M. Ruan, Y. Yin, Q. Song, K. Xie, C. Qin, M. Dong, Y. Zhou and J. Li, *RSC Adv.*, 2022, **12**, 378, DOI: **10.1039/d1ra06325a**.
3 P. Gong, J. Xie, D. Fang, X. Liu, F. He and F. Li, *Chem. Eng. J.*, 2019, **356**, 598–608, DOI: **10.1016/j.cej.2018.09.042**.
4 W. Shi, J. Zhang, X. Li, J. Zhou, Y. Pan, Q. Liu, Z. Xu and G. Qian, *Energy Fuels*, 2017, **31**, 11258–11265, DOI: **10.1021/acs.energyfuels.7b02230**.
5 K. Liu, H. He and B. Chu, *Chem. Eng. J.*, 2021, **423**, 130128, DOI: **10.1016/j.cej.2021.130128**.
6 X. Sun, Q. Liu, S. Liu, X. Zhang and S. Liu, *RSC Adv.*, 2021, **11**, 22780, DOI: **10.1039/d1ra03845a**.
7 S. Xiong, Y. Peng, D. Wang, N. Huang, Q. Zhang, S. Yang, J. Chen and J. Li, *Chem. Eng. J.*, 2020, **387**, 124090, DOI: **10.1016/j.cej.2020.124090**.
8 W. Wen, X. Wang, S. Jin and R. Wang, *RSC Adv.*, 2016, **6**, 74046–74052, DOI: **10.1039/C6RA18273A**.
9 J. Zhang, D. Tan, Q. Meng, X. Weng and Z. Wu, *Appl. Catal., B*, 2015, **172**, 18–26, DOI: **10.1016/j.apcatb.2015.02.006**.
10 C. Zhou, Z. Feng, Y. Zhang, L. Hu, R. Chen, B. Shan, H. Yin, W. Guo and A. Huang, *RSC Adv.*, 2015, **5**, 28054–28059, DOI: **10.1039/C5RA02344K**.
11 J. Yao, H. Lu, Y. Xiao, B. Hou, D. Li and L. Jia, *Catal. Commun.*, 2019, **128**, 105718, DOI: **10.1016/j.catcom.2019.105718**.
12 F. Zhang, X. Zhang, G. Jiang, N. Li, Z. Hao and S. Qu, *Chem. Eng. J.*, 2018, **348**, 831–839, DOI: **10.1016/j.cej.2018.05.050**.
13 H. Wu, M. He, W. Liu, L. Jiang, J. Cao, C. Yang, J. Yang, J. Peng, Y. Liu and Q. Liu, *J. Environ. Chem. Eng.*, 2021, **9**, 105426, DOI: **10.1016/j.jece.2021.105426**.
14 J. Yang, S. Ren, T. Zhang, Z. Su, H. Long, M. Kong and L. Yao, *Chem. Eng. J.*, 2020, **379**, 122398, DOI: **10.1016/j.cej.2019.122398**.
15 J. A. Onrubia-Calvo, B. Pereda-Ayo, U. De-La-Torre and J. R. González-Velasco, *Appl. Catal., B*, 2017, **213**, 198–210, DOI: **10.1016/j.apcatb.2017.04.068**.
16 Y. Wu, H. Liu, G. Li, L. Jin, X. Li, X. Ou, L. Dong, G. Jin and B. Li, *Appl. Surf. Sci.*, 2020, **508**, 145158, DOI: **10.1016/j.apsusc.2019.145158**.
17 B. Zhao, R. Ran, L. Sun, X. Guo, X. Wu and D. Weng, *RSC Adv.*, 2016, **6**, 69855–69860, DOI: **10.1039/C6RA12308B**.
18 C. Zhang, W. Hua, C. Wang, Y. Guo, Y. Guo, G. Lu and A. Baylet, *Appl. Catal., B*, 2013, **134–135**, 310–315, DOI: **10.1016/j.apcatb.2013.01.031**.
19 Y. Shao, X. Wang, M. Ao, C. Gong, G. Fan and H. Chen, *Front. Mater. Sci.*, 2012, **6**, 304–310, DOI: **10.1007/s11706-012-0179-z**.
20 G. Xiao, S. Xin, H. Wang, R. Zhang, Q. Wei and Y. Lin, *Ind. Eng. Chem. Res.*, 2019, **58**, 5388–5396, DOI: **10.1021/acs.iecr.8b05674**.
21 T. Wang, C. Li, L. Zhao, J. Zhang, S. Li and G. Zeng, *Appl. Surf. Sci.*, 2017, **400**, 227–237, DOI: **10.1016/j.apsusc.2016.12.192**.
22 H. Shu, Y. Liu and Y. Jia, *Sci. Total Environ.*, 2022, **820**, 152984, DOI: **10.1016/j.scitotenv.2022.152984**.
23 M. Thommes, K. Kaneko, A. V. Neimark, J. P. Olivier, F. Rodriguez-Reinoso, J. Rouquerol and K. S. W. Sing, *Pure Appl. Chem.*, 2015, **87**, 1051–1069, DOI: **10.1515/pac-2014-1117**.
24 G. Zhang, B. Lei, S. Chen, H. Xie and G. Zhou, *J. Environ. Chem. Eng.*, 2021, **9**, 105387, DOI: **10.1016/j.jece.2021.105387**.
25 C. Zhang, C. Wang, W. Zhan, Y. Guo, Y. Guo, G. Lu, A. Baylet and A. Giroir-Fendler, *Appl. Catal., B*, 2013, **129**, 509–516, DOI: **10.1016/j.apcatb.2012.09.056**.
26 G. Kim, S. Lee, K. Nam and S. Hong, *Appl. Surf. Sci.*, 2020, **507**, 145064, DOI: **10.1016/j.apsusc.2019.145064**.

27 S. Ni, X. Tang, H. Yi, F. Gao, C. Wang, Y. Shi, R. Zhang and W. Zhu, *J. Rare Earths*, 2022, **40**, 268–278, DOI: **10.1016/j.jre.2020.12.015**.
28 X. Wang, Y. Shi, S. Li and W. Li, *Appl. Catal., B*, 2018, **220**, 234–250, DOI: **10.1016/j.apcatb.2017.08.021**.
29 Sl. Ali, L. Chen, Z. Li, T. Zhang, R. Li, S. Bakhtiar, X. Leng, F. Yuan, X. Niu and Y. Zhu, *Appl. Catal., B*, 2018, **236**, 25–35, DOI: **10.1016/j.apcatb.2018.05.014**.
30 Q. Guo, W. Jing, Y. Hou, Z. Huang, G. Ma, X. Han and D. Sun, *Chem. Eng. J.*, 2015, **270**, 41–49, DOI: **10.1016/j.cej.2015.01.086**.
31 S. Feng, J. Liu and B. Gao, *Chem. Eng. J.*, 2022, **429**, 132302, DOI: **10.1016/j.cej.2021.132302**.
32 B. Shen, Y. Wang, F. Wang and T. Liu, *Chem. Eng. J.*, 2014, **236**, 171–180, DOI: **10.1016/j.cej.2013.09.085**.
33 Z. Wang, X. Xu, Y. Zhu, H. He, N. Wang, X. Yang and L. Liu, *Microporous Mesoporous Mater.*, 2022, **333**, 111720, DOI: **10.1016/j.micromeso.2022.111720**.
34 T. Wang, C. Li, L. Zhao, J. Zhang, S. Li and G. Zeng, *Appl. Surf. Sci.*, 2017, **400**, 227–237, DOI: **10.1016/j.apsusc.2016.12.192**.
35 M. Xing, Q. Sun, C. Zeng, H. Wang, D. Zhao, N. Zhang and S. Hong, *RSC Adv.*, 2017, **7**, 18830, DOI: **10.1039/c7ra00581d**.
36 P. Gong, J. Xie, D. Fang, X. Liu, F. He and F. Li, *Chem. Eng. J.*, 2019, **356**, 598–608, DOI: **10.1016/j.cej.2018.09.042**.
37 Q. Yan, Y. Gao, Y. Li, M. A. Vasiliades, S. Chen, C. Zhang, R. Gui, T. Zhu and A. M. Efstathiou, *Appl. Catal., B*, 2019, **255**, 117749, DOI: **10.1016/j.apcatb.2019.117749**.
38 P. Wang, S. Chen, S. Gao, J. Zhang, H. Wang and Z. Wu, *Appl. Catal., B*, 2018, **231**, 299–309, DOI: **10.1016/j.apcatb.2018.03.024**.
39 R. Zhang, W. Yang, N. Luo, P. Li, Z. Lei and B. Chen, *Appl. Catal., B*, 2014, **146**, 94–104, DOI: **10.1016/j.apcatb.2013.04.047**.
40 J. Wang, Z. Yan, L. Liu, Y. Chen, Z. Zhang and X. Wang, *Appl. Surf. Sci.*, 2014, **313**(13), 660–669, DOI: **10.1016/j.apsusc.2014.06.043**.
41 Q. Zhang, J. Fan, P. Ning, Z. Song, X. Liu, L. Wang, J. Wang, H. Wang and K. Long, *Appl. Surf. Sci.*, 2018, **435**, 1037–1045, DOI: **10.1016/j.apsusc.2017.11.180**.
42 L. Chen, J. Li and M. Ge, *Environ. Sci. Technol.*, 2010, **44**, 9590–9596, DOI: **10.1021/es102692b**.
43 S. Xie, L. Li, L. Jin, Y. Wu, H. Liu, Q. Qin, X. Wei, J. Liu, L. Dong and B. Li, *Appl. Surf. Sci.*, 2020, **515**, 146014, DOI: **10.1016/j.apsusc.2020.146014**.
44 F. Gao, C. Yang, X. Tang, H. Yi and C. Wang, *J. Environ. Sci.*, 2022, **113**, 204–218, DOI: **10.1016/j.jes.2021.05.032**.
45 Y. Shi, H. Yi, F. Gao, S. Zhao, Z. Xie and X. Tang, *J. Hazard. Mater.*, 2021, **413**, 125361, DOI: **10.1016/j.jhazmat.2021.125361**.
46 L. Chen, Z. Si, X. Wu and D. Weng, *ACS Appl. Mater. Interfaces*, 2014, **6**, 8134–8145, DOI: **10.1021/am5004969**.